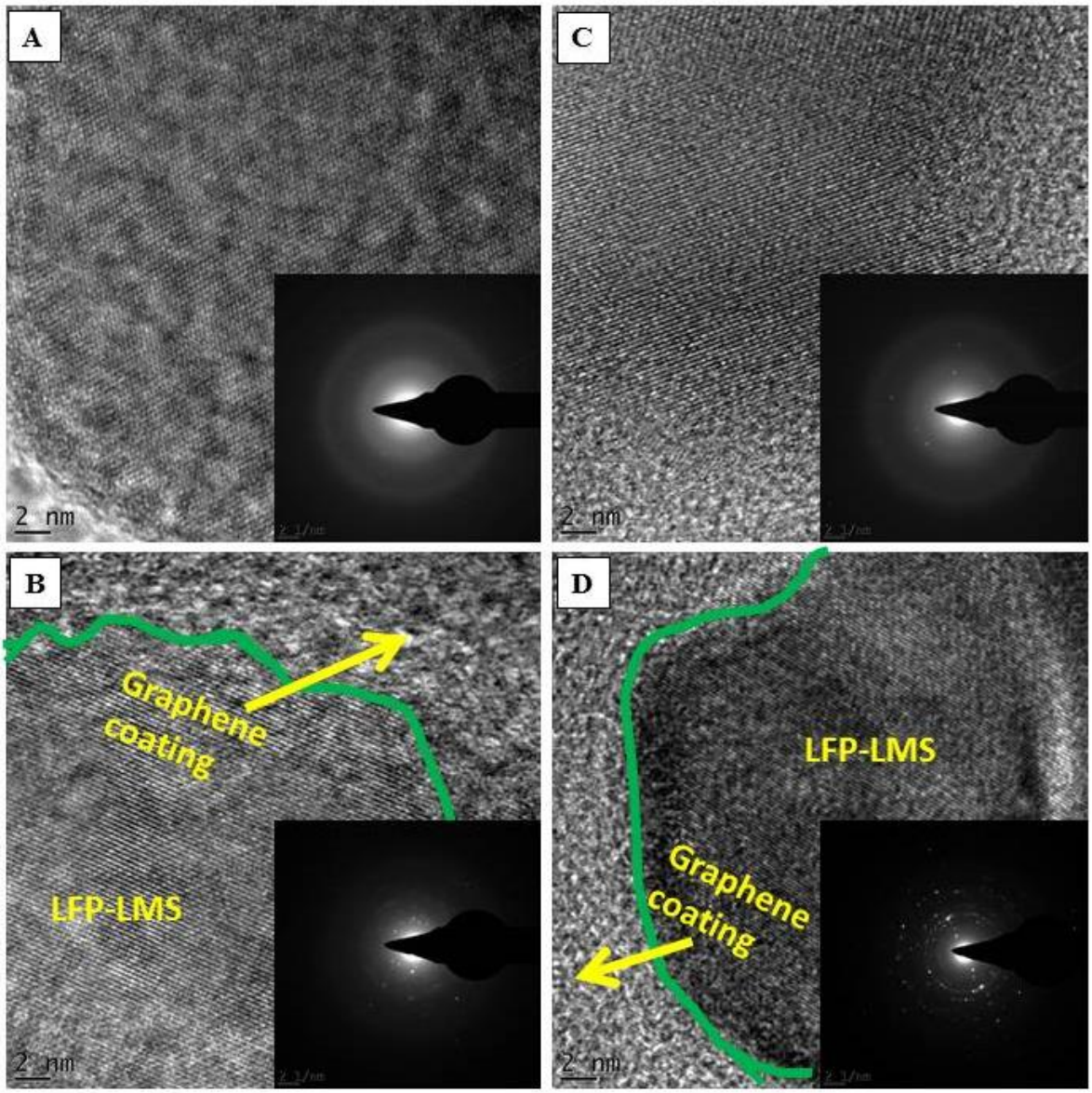

Figure 34: HRTEM images of (A) LFP-LMS HM, (B) LFP-LMS-G HM, (C) LFP-LMS SG and (D) LFP-LMS-G SG at low scale view of 2 ηm. The inserts are the SAED images corresponding to these hybrid cathode materials

Elemental mapping of the hybrid materials was confirmed again using EDS from HRTEM as indicated in Fig. 35. These finding are in agreement with the theory that there is better mixing with the *in situ* sol-get method compared to hand milling method. There is an almost even distribution of Fe and Mn in all the *in situ* sol-gel-prepared materials (Fig. 35 C and D) which is not the case in the materials prepared using the hand milling approach (Fig. 35 A and B. Again, the high content of O is attributed to oxygen in the PO_4 and SiO_4 groups.

The presence of Cu and Ni is caused by the copper-nickel grid used for analysis of the samples. There were also a few impurities of S and Ca in LFP-LMS HM and LFP-LMS SG, respectively.

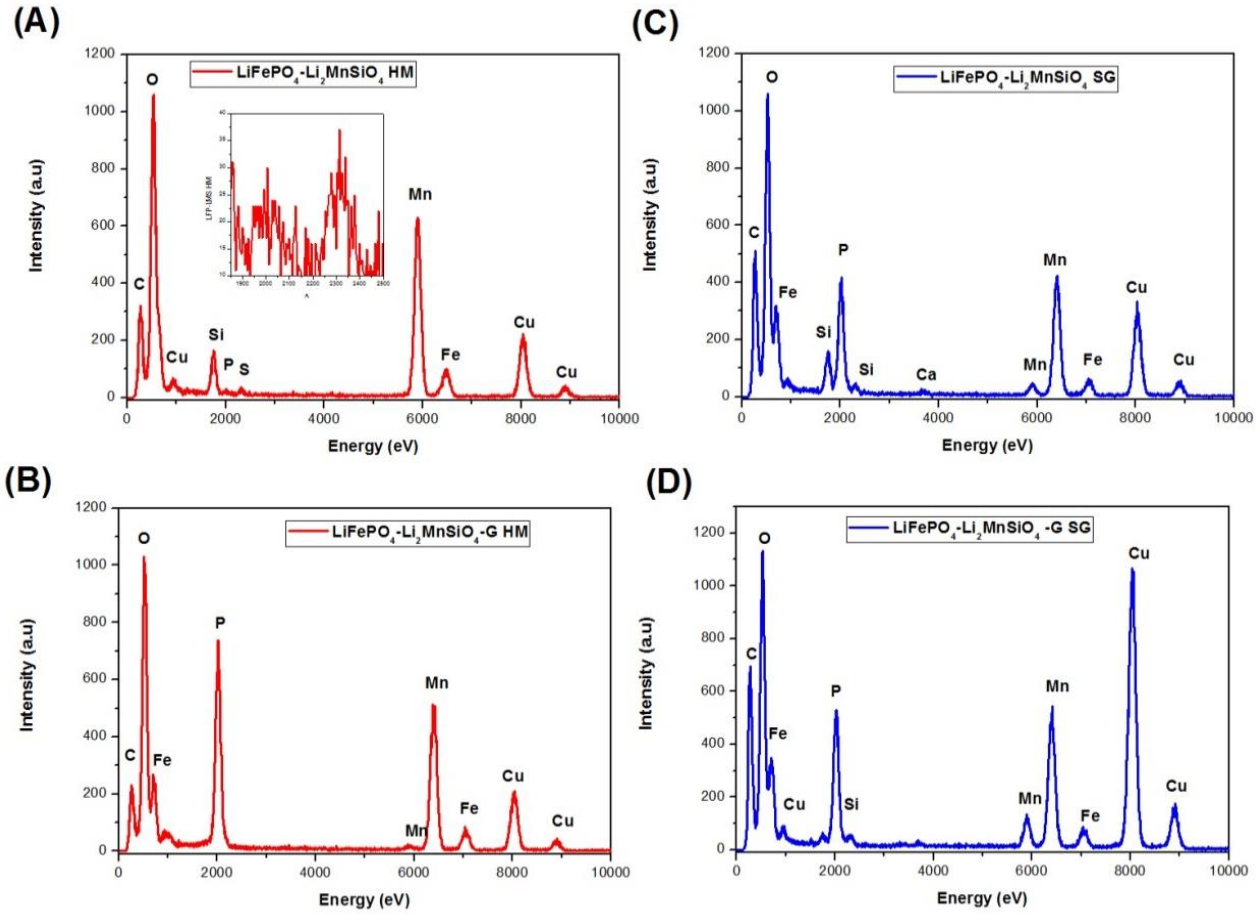

Figure 35: EDS spectra of all the synthesised hybrid cathode materials: where (A) and (B) represents the hand milling method and (C) and (D) the *in situ* sol-gel method

3.3.3. Small Angle Scattering X-Ray (SAXS)

The morphology and particle size distribution of the synthesised hybrid materials were further confirmed using SAXS as shown in Fig. 36. The slightly bell shaped peak of the pair-distance distribution function (PDDF) curves (Fig. 36 A) confirmed that these materials have an oblate/lamellar shape (described as spherical in HRSEM and TEM) having diameters of 36, 30, 37 and 23 ηm for LFP-LMS HM, LFP-LMS-G HM, LFP-LMS SG and LFP-LMS-G SG, respectively. Indeed, the presence of graphene in both hybrid materials played a

http://etd.uwc.ac.za

significant role in particle size reduction, more especially in the LFP-LMS-G SG. The particle size distribution curves (Fig. 36 B) show that the hybrid cathode materials had a distribution in their particle sizes from 5 to 65 ηm.

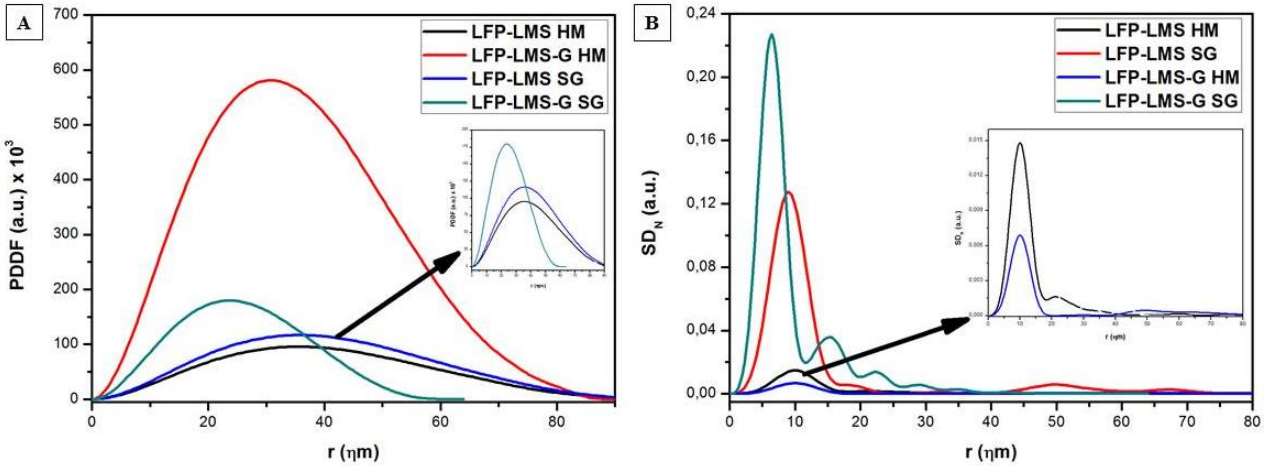

Figure 36: SAXS data: (A) PDDF (insert: the shape of the seemingly broad curves without the influence of LFP-LMS-G HM) and (B) particle size distribution curves (inset: zoomed area of the curves) of the prepared hybrid cathode materials

3.3.4. Fourier Transform Infrared Spectroscopy (FTIR)

UNIVERSITY of the
WESTERN CAPE

Figure 37 shows the FTIR spectra of the LFP-LMS HM, LFP-LMS-G HM, LFP-LMS SG and LFP-LMS-G SG hybrid cathode materials. The hybrid cathode materials show a set of three bands in the region between 400 and 1600 cm^{-1}. In the low wavenumber region, the band at 455 cm^{-1} is attributed to the local Li-ion environment or rather Li-ion motion form $LiFePO_4$ and Li_2MnSiO_4 in the hybrid materials [9, 43]. The second band appearing between 535 and 665 cm^{-1} is ascribed to the bending vibrations of the $[PO_4]^{3-}$ unit of $LiFePO_4$ as well as the ν_1 and ν_4 modes of $[SiO_4]$ in Li_2MnSiO_4 [10]. In the high wavenumber region, the band between 940 and 1240 cm^{-1} was observed and is due to the stretching vibrations of $[PO_4]^{3-}$ and the $\nu_{1,}$ and ν_4 modes of $[SiO_4]$ [8, 9]. The LFP-LMS HM and LFP-LMS-G HM hybrid cathode materials contained Li_2SiO_3 impurity observed at 862 cm^{-1}. However, this impurity was not observed in LFP-LMS SG and LFP-LMS-G SG hybrid cathodes.

http://etd.uwc.ac.za

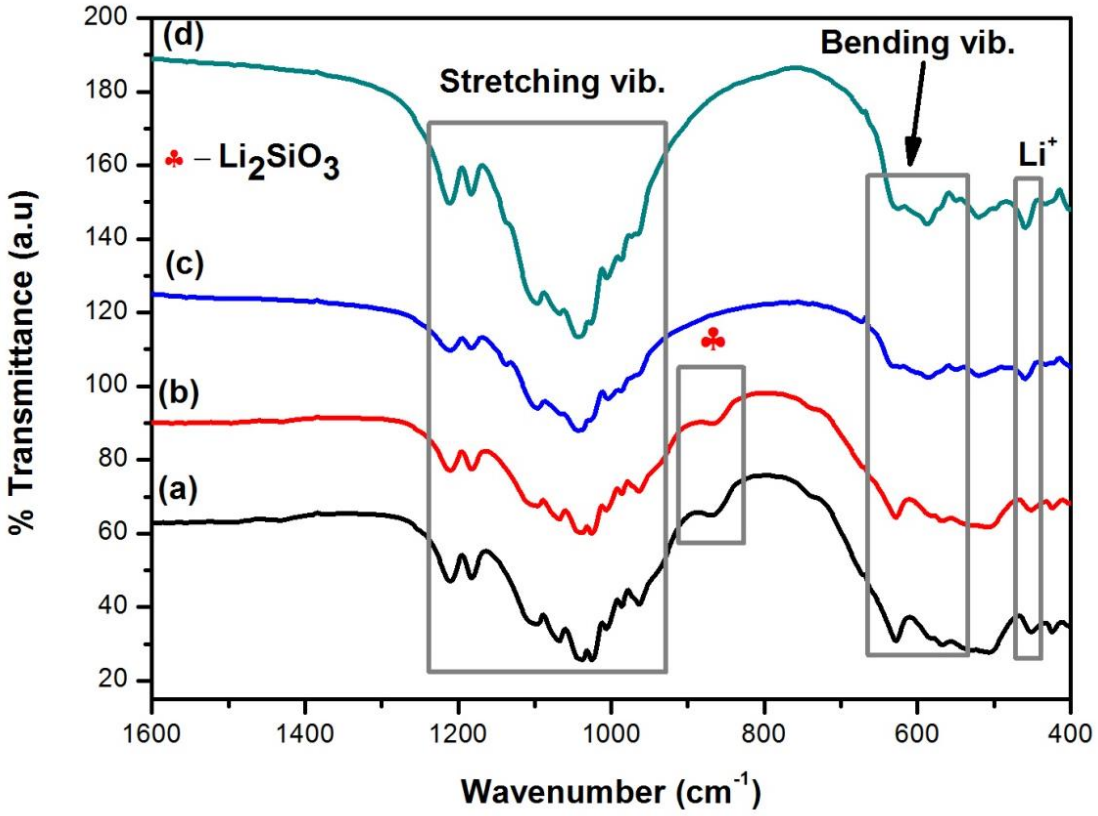

Figure 37: FTIR spectra of (a) LFP-LMS HM, (b) LFP-LMS-G HM, (c) LFP-LMS SG and (d) LFP-LMS-G SG

UNIVERSITY of the
WESTERN CAPE

3.3.5. X-Ray Diffraction

The structure of the hybrid cathode materials was studied using X-ray diffraction in the 2Θ range from 10 to 80 º as shown in Fig. 38. The sharp diffraction peaks are a clear indication that the powder samples have a crystalline structure. There are no obvious changes in the diffraction peak positions of the LFP-LMS HM and LFP-LMS-G HM (Fig. 38 A and B) with respect to those of the pristine materials (Fig. 16, Section 3.1.5). However, there are changes observed in the diffraction patterns of LFP-LMS SG and LFP-LMS-G SG shown by the disappearance of two intense peaks at 2Θ = 19 and 44 º. An explanation for the disappearance of these diffraction peaks in the hybrid material is that the pristine LMS was calcined separately before being incorporated into the hybrid cathodes. Therefore, calcining the material again at high temperatures during the preparation of the hybrid might have caused structural changes; hence the disappearance of the two peaks. These results suggest that the hybrid cathode materials prepared using the *in situ* sol-gel method had diffraction patterns

http://etd.uwc.ac.za

similar to those of LFP more than LMS. The hybrid cathodes prepared using the hand milling approach on the other hand showed a pattern that resembles the presence of both pristine cathode materials.

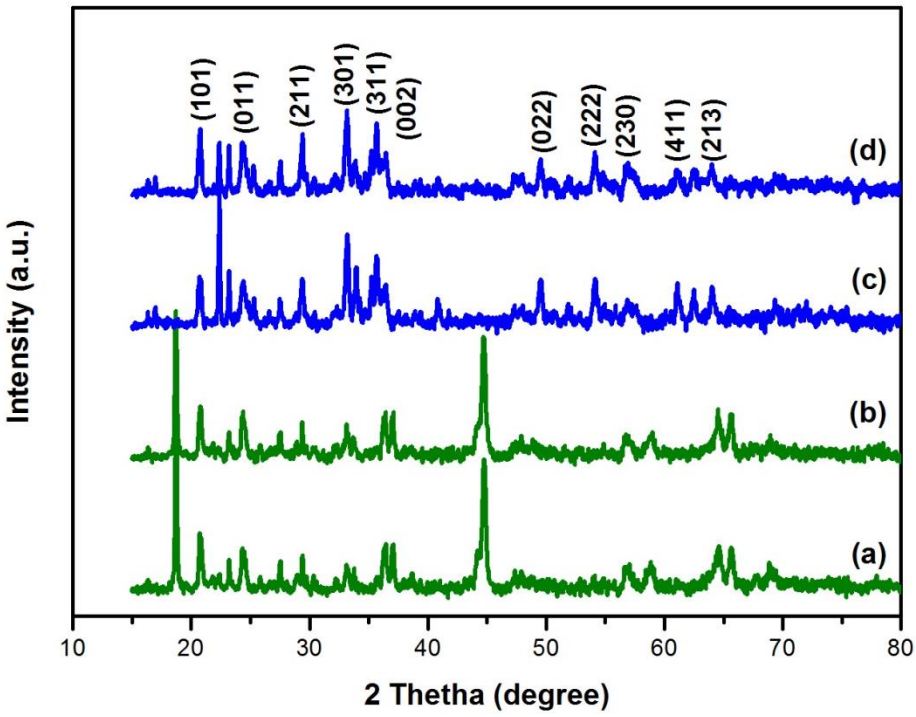

Figure 38: X-Ray diffraction patterns of (a) LFP-LMS HM, (b) LFP-LMS-G HM, (c) LFP-LMS SG and (d) LFP-LMS-G SG

UNIVERSITY of the
WESTERN CAPE

3.3.6. Thermogravimetric (TG) Analysis

Figure 39 shows the TG analysis of the different hybrid cathode materials under N_2 atmosphere from room temperature to 900 ºC. As can be seen from this Figure, the total weight loss of LFP-LMS HM, LFP-LMS-G HM, LFP-LMS SG and LFP-LMS-G SG were 5.9 %, 9.9%, 4.5 % and 3.4 %, respectively. The LFP-LMS-G SG has the highest thermal stability with only just 3.4 % weight loss which is ascribed to the crystallization of this material [15]. In contrast, LFP-LMS-G HM showed inferior thermal stabilities compared to other materials with a weight loss of 9.9 %. It can be observed that both hand-mill-prepared hybrid cathode materials showed weight gain from room temperature to approximately 450 ºC compared to those prepared via the *in situ* sol-gel approach which only showed a weight

http://etd.uwc.ac.za

decrease with an increase in temperature. The hand-mill-prepared hybrid cathodes were prepared in open-air environment therefore the weight gain could be caused by the reaction of absorbed moisture and the N_2 atmosphere inside the furnace.

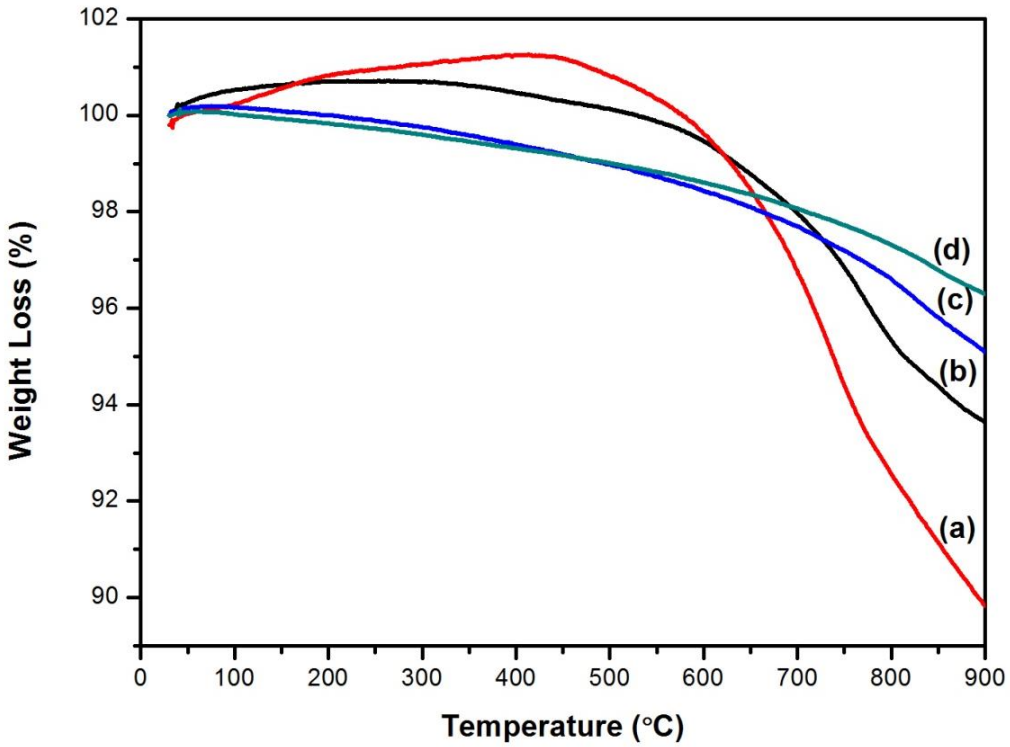

Figure 39: TG curves of the synthesised (a) LFP-LMS-G HM, (b) LFP-LMS HM, (c) LFP-LMS SG and (d) LFP-LMS-G SG hybrid cathode materials

UNIVERSITY of the
WESTERN CAPE

3.3.7. Electrochemistry

3.3.7.1. Cyclic Voltammetry

The electrochemical behaviour of the synthesised hybrid cathode materials; LFP-LMS HM, LFP-LMS-G HM, LFP-LMS SG and LFP-LMS-G SG were studied using cyclic voltammetry and the results are shown in Fig. 40. Figure 40 A shows three redox peaks observed for during the oxidation and reduction scans of LFP-LMS HM and LFP-LMS-G HM in the given potential window between -1000 and 800 mV. The absence of the oxidation peak in iron is associated with the used electrolyte. The peak potentials corresponding to these peaks are shown in Table 7. It is clear that the graphenised hybrid cathode material has a high current compared to LFP-LMS hybrid cathode. The high current of this material is associated with an

http://etd.uwc.ac.za

improved capacity attributed to the presence of graphene. The capacity values for these materials were calculated the same way as the pristine materials and are tabulated in Table 8.

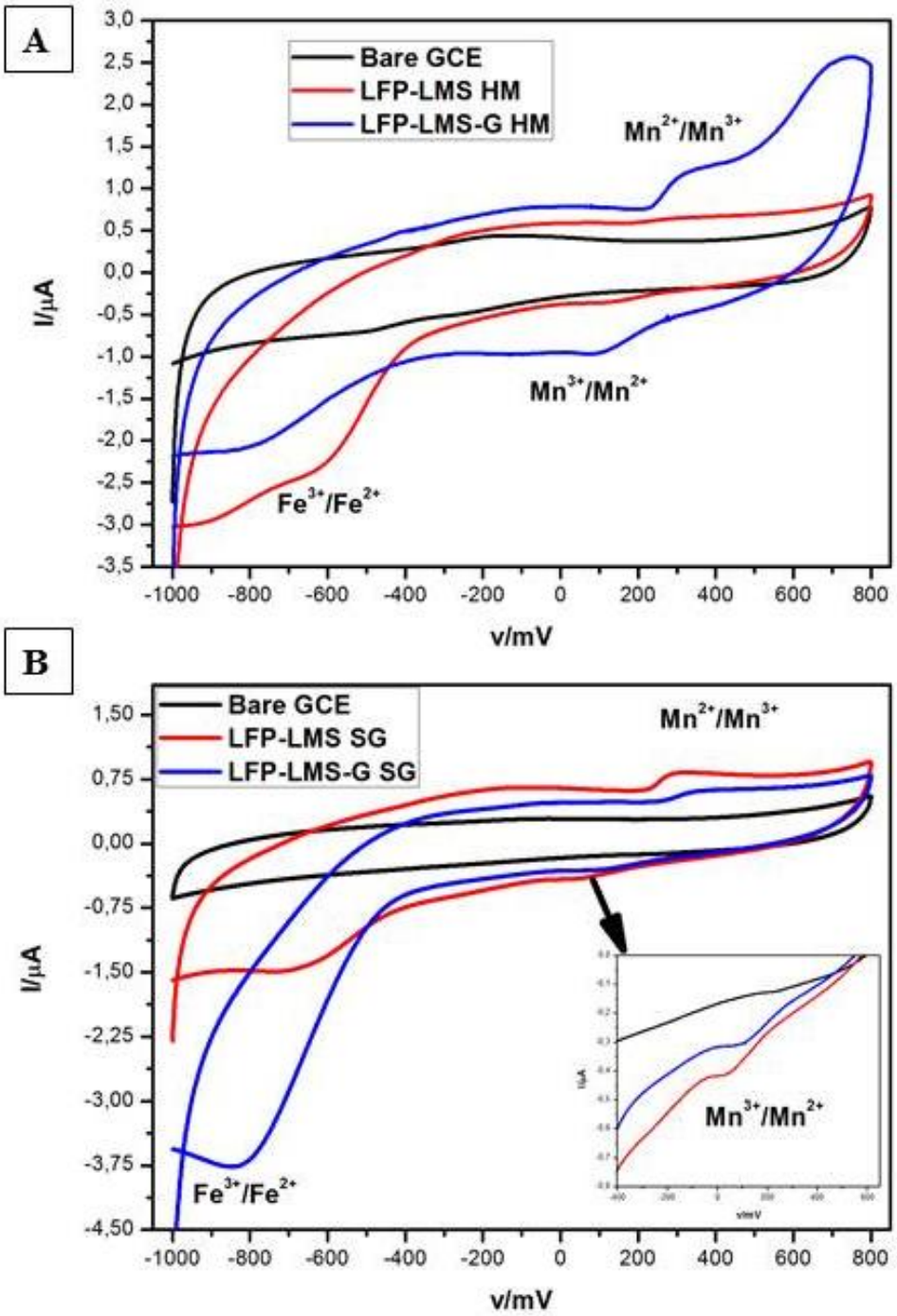

Figure 40: Cyclic voltammograms of (A) hybrid cathodes prepared via the hand milling and (B) *in situ* sol-gel methods in 1.0 M $LiClO_4$ in the potential window between -1000 and 800 mV, at a scan rate of 05 mV s^{-1}

http://etd.uwc.ac.za

Table 7: The observed peaks characterised by these peak potentials and currents for the prepared hybrid cathode materials

Materials	E_{pa}/mV	I_{pa}/μA	E_{pc1}/mV	I_{pc1}/μA	E_{pc2}/mV	I_{pc2}/μA
LFP-LMS HM	285	0.64	108	-0.36	-800	-2.09
LFP-LMS-G HM	331	1.20	78	-0.96	-646	-2.40
LFP-LMS SG	348	0.61	35	-0.42	-702	-1.49
LFP-LMS-G SG	295	0.82	89	-0.31	-840	-3.76

Figure 40 B shows cyclic voltamogramms for LFP-LMS and LFP-LMS-G hybrid cathode materials prepared using the *in situ* sol-gel approach. These materials show the same shape and number of peaks as those prepared via the hand milling method. The corresponding peak potentials and calculated capacities for these materials are also presented in Tables 7 and 8, respectively. The results clearly show that both graphenised LFP-LMS hybrid cathode materials offer higher capacities than those of LFP-LMS hybrid cathodes and this is associated with the presence of graphene nanosheets in these samples. The LFP-LMS-G SG hybrid cathode showed the highest specific capacity of 4.056 mA h g^{-1} compared to LFP-LMS-G HM with 3.408 mA h g^{-1}. These results clearly show that the *in situ* sol-gel method yielded better performing hybrid cathodes than the hand milling method.

Table 8: Calculated capacities for the hybrid cathode materials

Materials	Specific capacity/mA h g^{-1}
LFP-LMS HM	2.804
LFP-LMS-G HM	3.408
LFP-LMS SG	2.524
LFP-LMS-G SG	4.056

http://etd.uwc.ac.za

The cyclic voltammograms of LFP-LMS-G HM and LFP-LMS-G SG at different scan rates (01 to 09 mV s^{-1}) are shown in Fig. 41. Both graphenised hybrid cathodes exhibit an irreversible behaviour supported by the differences between peak potentials which increases with an increase in scan rates. On the contrary, the reduction peak of iron in LFP-LMS-G HM (Fig 41 A) is less pronounced compared to that of LFP-LMS-G SG (Fig 41 B) which is associated with the different methods used for preparation of these hybrid cathodes. As a result, the more pronounced reduction peak of iron in LFP-LMS-G SG overshadows the redox pair of manganese in this hybrid cathode.

UNIVERSITY of the
WESTERN CAPE

http://etd.uwc.ac.za

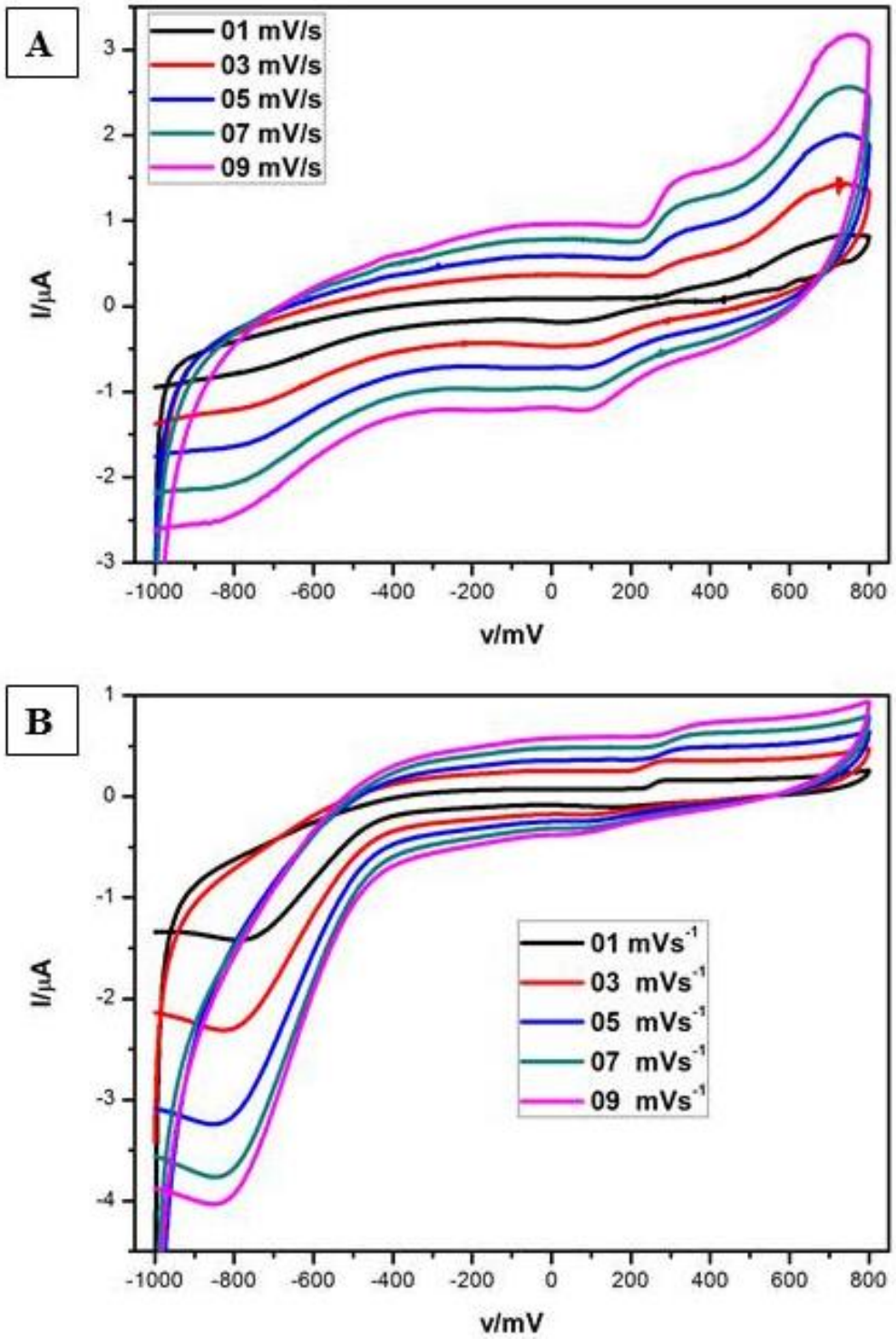

Figure 41: Cyclic voltammograms for (A) LFP-LMS-G HM and (B) LFP-LMS-G SG hybrid cathodes in 1.0 M $LiClO_4$ at different scan rates between 01 - 09 mV s^{-1}

http://etd.uwc.ac.za

3.3.7.2. Electrochemical Impedance Spectroscopy

EIS studies for the hybrid cathode materials were discussed using the Nyquist plots (Fig. 42) and Bode plots (Fig. 43). The Nyquist plots for these materials are represented in Fig. 42 A and B and it can be clearly observed that these plots only show an inclined line without any semi-circle (see inset graphs), which is characteristic of a capacitive behaviour. This line is attributed to the Warburg impedance associated with Li-ion diffusion in the bulk electrode, which suggests that the kinetics of the intercalation/de-intercalation process is controlled by the diffusion process [31]. These plots were best fitted using the modified Randles equivalent circuits shown in Fig. 42 C and D, which corresponds to the unmodified and graphenised hybrid cathodes, respectively. The obtained values for the fitted parameters are shown in Table 9. It can be observed that both graphenised hybrid cathodes show a low solution resistance and low charge transfer resistance which is an indication that these materials have fast kinetics compared to the unmodified hybrid cathodes. Further comparison between the two graphenised cathodes shows that the one prepared via the *in situ* sol-gel method has the fastest kinetics, which can be attributed to small particle size and coating with graphene nanosheets.

UNIVERSITY of the
WESTERN CAPE

http://etd.uwc.ac.za

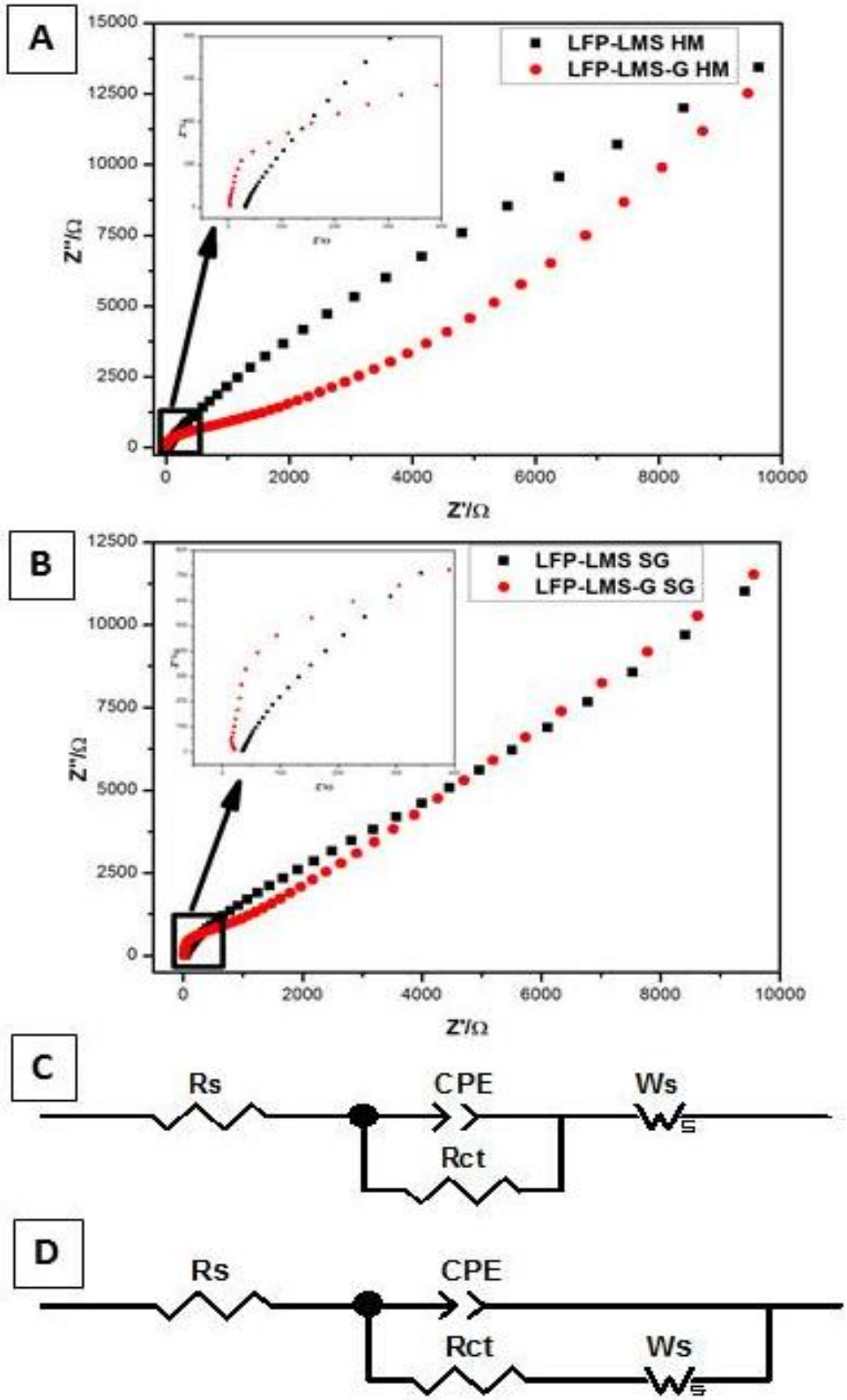

Figure 42: Nyquist plots for hybrid cathode materials prepared via (A) the hand milling method and (B) *in situ* sol-gel method and the corresponding Randles equivalent circuits (C) and (D) for the LFP-LMS and LFP-LMS-G hybrid cathode materials, respectively

http://etd.uwc.ac.za

Table 9: The fitted parameters of the Randles equivalent circuit for the hybrid cathode materials

Material	R_s/Ω	CPE/F	R_{ct}/Ω	$W_s/\Omega\ s^{-1/2}$
LFP-LMS HM	28.01	5.09×10^{-6}	54589	0.147
LFP-LMS-G HM	5.42	4.98×10^{-8}	586.3	0.857
LFP-LMS SG	31.56	5.11×10^{-6}	3954	0.913
LFP-LMS-G SG	2.73	2.24×10^{-9}	389.5	0.632

The high performance of the graphenised hybrid cathodes is further highlighted using the Bode plots as shown in Fig. 43. The LFP-LMS-G HM exhibited a higher phase angle max. at 96.6 º and low impedance of 3.97 Ω compared to the phase angle max. at 69.4 º and impedance of 4.24 Ω for LFP-LMS HM. In addition, the LFP-LMS-G SG had the highest phase angle max. at 113.9 º with a slightly high impedance of 4.44 Ω compared to LFP-LMS SG with a phase angle max at 66.4 º and impedance of 4.11 Ω. The LFP-LMS-G HM hybrid shows fast kinetics while the LFP-LMS-G SG has conducting properties attributed to low impedance and higher phase angle max., respectively.

UNIVERSITY of the
WESTERN CAPE

http://etd.uwc.ac.za

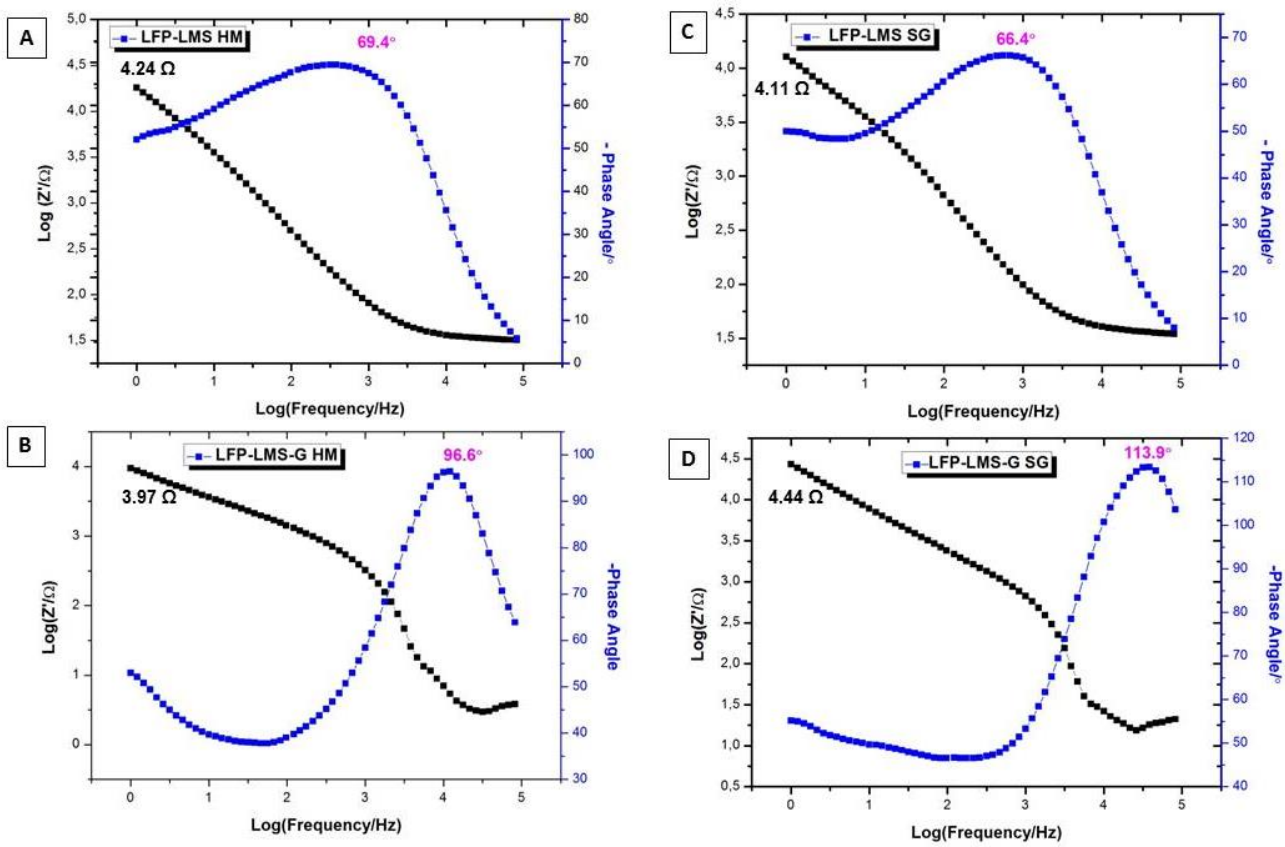

Figure 43: Bode plots for (A) LFP-LMS HM, (B) LFP-LMS-G HM, (C) LFP-LMS SG and (D) LFP-LMS-G SG hybrid cathode materials

UNIVERSITY of the
WESTERN CAPE

The kinetics of these hybrid cathodes were determined using the plots of Z' vs $\omega^{-1/2}$ as shown by Fig. 44. The slope of these plots gave the Warburg coefficients (σ) which were used to calculate the apparent diffusion coefficients (D_{app}) using the following Equation:

$$D_{app} = \left(\frac{\sqrt{2}RT}{\sigma n^2 F^2 AC} \right)^2 \qquad (24)$$

where A is the area of the GCE = 0.071 cm^2, C is the concentration of Li-ions = 4.943 x 10^{-5}, 4.943 x 10^{-5}, 4.472 x 10^{-5} and 4.707 x 10^{-5} mol cm^{-3} for LFP-LMS HM, LFP-LMS-G HM, LFP-LMS SG and LFP-LMS-G SG, respectively. The obtained σ values from Z' vs $\omega^{-1/2}$ are shown in Fig. 44 and Table 10. The D_{app} for the graphenised LFP-LMS is higher than that of LFP-LMS hybrid cathode prepared via the hand milling method. However, graphenised LFP-LMS has a slightly lower D_{app} compared to LFP-LMS prepared via the *in situ* sol-gel method.

http://etd.uwc.ac.za

The slow diffusion of Li-ions in graphenised LFP-LMS might be caused by 1-D paths in the structure of LFP in the hybrid.

Table 10: Kinetic parameters of LFP-LMS HM, LFP-LMS-G HM, LFP-LMS SG and LFP-LMS-G SG obtained from EIS plots of these electrodes at 298.15 K

Cathode Material	$\sigma/\Omega\ s^{-1/2}$	$D_{app}/cm^2\ s^{-1}$
LFP-LMS HM	54196.24	2.450×10^{-13}
LFP-LMS-G HM	21380.71	1.574×10^{-12}
LFP-LMS SG	34129.80	7.547×10^{-13}
LFP-LMS-G SG	72038.91	1.529×10^{-13}

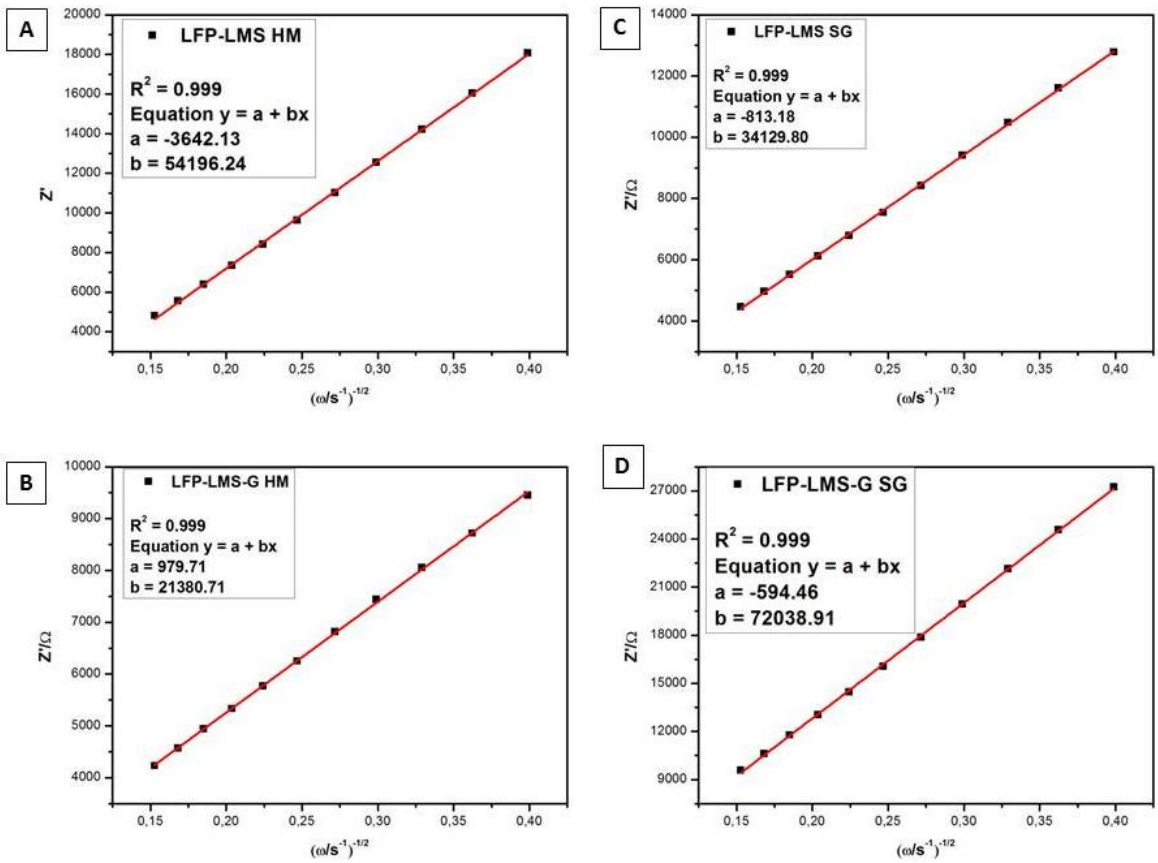

Figure 44: *Z'* vs $\omega^{-1/2}$ curves for (A) LFP-LMS HM, (B) LFP-LMS-G HM, (C) LFP-LMS SG and LFP-LMS-G SG

http://etd.uwc.ac.za

REFERENCES

1. Babbar, P., B. Tiwari, B. Purohit, A. Ivanishchev, A. Churikov, and A. Dixit, *Charge/discharge characteristics of Jahn–Teller distorted nanostructured orthorhombic and monoclinic Li_2MnSiO_4 cathode materials.* RSC Advances, 2017. **7**(37): p. 22990-22997.
2. Egerton, R.F., *Physical principles of electron microscopy: An introduction to TEM, SEM, and AEM*. 2005, 233 Spring Street, New York, NY 10013, United States of America: Springer Science + Business Media Inc. 202.
3. Chen, R., T. Zhao, X. Zhang, L. Li, and F. Wu, *Advanced cathode materials for lithium-ion batteries using nanoarchitectonics.* Nanoscale Horizons, 2016. **1**(6): p. 423-444.
4. Schnablegger, H. and Y. Singh, *The SAXS guide: Getting acquainted with the principles*. 3rd ed. 2011, A-8054 Graz, Austria: Austria: Anton Paar GmbH. 122.
5. Li, T., A.J. Senesi, and B. Lee, *Small angle X-ray scattering for nanoparticle research.* Chemical reviews, 2016. **116**(18): p. 11128-11180.
6. Ramachandran, R., M. Saranya, V. Velmurugan, B.P. Raghupathy, S.K. Jeong, and A.N. Grace, *Effect of reducing agent on graphene synthesis and its influence on charge storage towards supercapacitor applications.* Applied Energy, 2015. **153**: p. 22-31.
7. Miao, C., P. Bai, Q. Jiang, S. Sun, and X. Wang, *A novel synthesis and characterization of $LiFePO_4$ and $LiFePO_4/C$ as a cathode material for lithium-ion battery*. Journal of Power Sources, 2014. **246**: p. 232-238.
8. Mohan, E.H., V. Siddhartha, R. Gopalan, T.N. Rao, and D. Rangappa, *Urea and sucrose assisted combustion synthesis of $LiFePO_4/C$ nano-powder for lithium-ion battery cathode application.* AIMS Materials Science, 2014. **1**(4): p. 191-201.
9. Luo, S., M. Wang, and W. Sun, *Fabricated and improved electrochemical properties of Li_2MnSiO_4 cathodes by hydrothermal reaction for Li-ion batteries.* Ceramics International, 2012. **38**(5): p. 4325-4329.
10. Xie, M., R. Luo, R. Chen, F. Wu, T. Zhao, Q. Wang, and L. Li, *Template-Assisted Hydrothermal Synthesis of Li_2MnSiO_4 as a Cathode Material for Lithium Ion Batteries.* ACS applied materials & interfaces, 2015. **7**(20): p. 10779-10784.

UNIVERSITY of the
WESTERN CAPE

http://etd.uwc.ac.za

11. Zaghib, K., A. Ait Salah, N. Ravet, A. Mauger, F. Gendron, and C.M. Julien, *Structural, magnetic and electrochemical properties of lithium iron orthosilicate.* Journal of Power Sources, 2006. **160**(2): p. 1381-1386.

12. Zhang, Z., X. Liu, L. Wang, Y. Wu, H. Zhao, and B. Chen, *Synthesis of Li_2FeSiO_4/C nanocomposite via a hydrothermal-assisted sol–gel process.* Solid State Ionics, 2015. **276**: p. 33-39.

13. Liu, Y., C. Cao, and J. Li, *Enhanced electrochemical performance of carbon nanospheres–$LiFePO_4$ composite by PEG based sol–gel synthesis.* Electrochimica Acta, 2010. **55**(12): p. 3921-3926.

14. Gong, H., H. Xue, T. Wang, and J. He, *In-situ synthesis of monodisperse micro-nanospherical $LiFePO_4$/carbon cathode composites for lithium-ion batteries.* Journal of Power Sources, 2016. **318**: p. 220-227.

15. Gao, M., N. Liu, Z. Li, W. Wang, C. Li, H. Zhang, Y. Chen, Z. Yu, and Y. Huang, *A gelatin-based sol–gel procedure to synthesize the $LiFePO_4$/C nanocomposite for lithium ion batteries.* Solid State Ionics, 2014. **258**: p. 8-12.

16. Kim, J.-K., J.-W. Choi, G.S. Chauhan, J.-H. Ahn, G.-C. Hwang, J.-B. Choi, and H.-J. Ahn, *Enhancement of electrochemical performance of lithium iron phosphate by controlled sol–gel synthesis.* Electrochimica Acta, 2008. **53**(28): p. 8258-8264.

17. Zhao, X., D.-H. Baek, J. Manuel, M.-Y. Heo, R. Yang, J.K. Ha, H.-S. Ryu, H.-J. Ahn, K.-W. Kim, and K.-K. Cho, *Electrochemical properties of magnesium doped $LiFePO_4$ cathode material prepared by sol–gel method.* Materials Research Bulletin, 2012. **47**(10): p. 2819-2822.

18. Tian, Z., Z. Zhou, S. Liu, F. Ye, and S. Yao, *Enhanced properties of olivine $LiFePO_4$/graphene co-doped with Nb^{5+} and Ti^{4+} by a sol–gel method.* Solid State Ionics, 2015. **278**: p. 186-191.

19. Wang, M., M. Yang, L. Ma, X. Shen, and X. Zhang, *Structural evolution and electrochemical performance of Li_2MnSiO_4/C nanocomposite as cathode material for li-ion batteries.* Journal of nanomaterials, 2014. **2014**: p. 4.

20. Belharouak, I., A. Abouimrane, and K. Amine, *Structural and electrochemical characterization of Li_2MnSiO_4 cathode material.* The Journal of Physical Chemistry C, 2009. **113**(48): p. 20733-20737.

21. Gummow, R.J. and Y. He, *Mesoporous manganese-deficient lithium manganese silicate cathodes for lithium-ion batteries.* RSC Advances, 2014. **4**(23): p. 11580-11584.

UNIVERSITY of the WESTERN CAPE
http://etd.uwc.ac.za

22. Dominko, R., M. Bele, A. Kokalj, M. Gaberscek, and J. Jamnik, *Li_2MnSiO_4 as a potential Li-battery cathode material.* Journal of Power Sources, 2007. **174**(2): p. 457-461.

23. Aravindan, V., K. Karthikeyan, S. Ravi, S. Amaresh, W.S. Kim, and Y.S. Lee, *Adipic acid assisted sol–gel synthesis of Li_2MnSiO_4 nanoparticles with improved lithium storage properties.* Journal of Materials Chemistry, 2010. **20**(35): p. 7340-7343.

24. Zhang, Q., Q. Zhuang, S. Xu, X. Qiu, Y. Cui, Y. Shi, and Y. Qiang, *Synthesis and characterization of pristine Li_2MnSiO_4 and Li_2MnSiO_4/C cathode materials for lithium ion batteries.* Ionics, 2012. **18**(5): p. 487-494.

25. Arroyo-deDompablo, M., R. Dominko, J. Gallardo-Amores, L. Dupont, G. Mali, H. Ehrenberg, J. Jamnik, and E. Moran, *On the energetic stability and electrochemistry of Li_2MnSiO_4 polymorphs.* Chemistry of Materials, 2008. **20**(17): p. 5574-5584.

26. Hwang, C., T. Kim, J. Shim, K. Kwak, K.M. Ok, and K.-K. Lee, *Fast ultrasound-assisted synthesis of Li_2MnSiO_4 nanoparticles for a lithium-ion battery.* Journal of Power Sources, 2015. **294**: p. 522-529.

27. Huang, Z., P. Luo, and D. Wang, *Preparation and characterization of core-shell structured $LiFePO_4$/C composite using a novel carbon source for lithium-ion battery cathode.* Journal of Physics and Chemistry of Solids, 2017. **102**: p. 115-120.

28. Jiang, J. and J.R. Dahn, *ARC studies of the thermal stability of three different cathode materials: $LiCoO_2$; $Li[Ni_{0.1}Co_{0.8}Mn_{0.1}]O_2$; and $LiFePO_4$, in $LiPF_6$ and LiBoB EC/DEC electrolytes.* Electrochemistry Communications, 2004. **6**(1): p. 39-43.

29. Hlongwa, N.W., *Nanoparticles-infused lithium manganese phosphate coated with magnesium-gold composite thin film-a possible novel material for lithium ion battery olivine cathode*. 2014, University of the Western Cape: Bellville, Cape Town, South Africa p. 90.

30. Ndipingwi, M.M., *Designing next generation high energy density lithium-ion battery with manganese orthosilicate-capped alumina nanofilm*. 2015, Universirty of the Western Cape: Bellville, Cape Town, South Africa. p. 109.

31. Ikpo, C.O., *Development of high performance composite lithium ion battery cathode systems with carbon nanotubes functionalised with bimetallic inorganic nanocrystal alloys*. 2011, University of Western Cape: Bellville, Cape Town, South Africa. p. 156.

32. Huang, X., J. Tu, C. Zhang, and J. Xiang, *Net-structured NiO–C nanocomposite as Li-intercalation electrode material.* Electrochemistry Communications, 2007. **9**(5): p. 1180-1184.

UNIVERSITY of the
WESTERN CAPE
http://etd.uwc.ac.za

33. Hummers Jr, W.S. and R.E. Offeman, *Preparation of graphitic oxide.* Journal of the American Chemical Society, 1958. **80**(6): p. 1339-1339.

34. Shahriary, L. and A.A. Athawale, *Graphene oxide synthesized by using modified hummers approach.* Int. J. Renew. Energy Environ. Eng, 2014. **2**(01): p. 58-63.

35. Hanifah, M., J. Jaafar, M. Aziz, A. Ismail, M. Rahman, and M. Othman, *Synthesis of graphene oxide nanosheets via modified hummers' method and its physicochemical properties.* Jurnal Teknologi, 2015. **74**(1): p. 189-192.

36. Kellici, S., J. Acord, J. Ball, H.S. Reehal, D. Morgan, and B. Saha, *A single rapid route for the synthesis of reduced graphene oxide with antibacterial activities.* RSC Advances, 2014. **4**(29): p. 14858-14861.

37. Çiplak, Z., N. Yildiz, and A. Çalimli, *Investigation of graphene/Ag nanocomposites synthesis parameters for two different synthesis methods.* Fullerenes, Nanotubes and Carbon Nanostructures, 2015. **23**(4): p. 361-370.

38. Aslam, M., M. Kalyar, and Z. Raza, *Synthesis and structural characterization of separate graphene oxide and reduced graphene oxide nanosheets.* Materials Research Express, 2016. **3**(10): p. 105036.

39. Ren, P.-G., D.-X. Yan, X. Ji, T. Chen, and Z.-M. Li, *Temperature dependence of graphene oxide reduced by hydrazine hydrate.* Nanotechnology, 2010. **22**(5): p. 055705.

40. Wang, G., J. Yang, J. Park, X. Gou, B. Wang, H. Liu, and J. Yao, *Facile synthesis and characterization of graphene nanosheets.* The Journal of Physical Chemistry C, 2008. **112**(22): p. 8192-8195.

41. Yaragalla, S., A. Meera, N. Kalarikkal, and S. Thomas, *Chemistry associated with natural rubber–graphene nanocomposites and its effect on physical and structural properties.* Industrial Crops and Products, 2015. **74**: p. 792-802.

42. Haubner, K., J. Murawski, P. Olk, L.M. Eng, C. Ziegler, B. Adolphi, and E. Jaehne, *The route to functional graphene oxide.* ChemPhysChem, 2010. **11**(10): p. 2131-2139.

43. Miao, C., P. Bai, Q. Jiang, S. Sun, and X. Wang, *A novel synthesis and characterization of $LiFePO_4$ and $LiFePO_4/C$ as a cathode material for lithium-ion battery.* Journal of Power Sources, 2014. **246**: p. 232-238.

UNIVERSITY of the
WESTERN CAPE

http://etd.uwc.ac.za

CHAPTER 4

4. Conclusion and Recommendations

4.1. Conclusion

Blending of individual cathode materials has unique advantages over the use of a single cathode material in Li-ion battery applications. This study focused on the preparation and characterisation of graphenised lithium iron phosphate-lithium manganese silicate (LFP-LMS-G), and lithium iron phosphate-lithium manganese silicate (LFP-LMS) which were prepared using two different methods; hand milling and *in situ* sol-gel. The precursors for the hybrid cathodes; $LiFePO_4$ (LFP), Li_2MnSiO_4 (LMS) and graphene nanosheets were prepared and characterized using various analytical techniques in order to probe their chemical, electrochemical and physical properties.

Both pristine LFP and LMS cathode materials were prepared using the sol-gel approach and the obtained nanoparticles were spherical in shape with minimal agglomeration. These nanoparticles had an average size of 35 and 40 nm corresponding to LFP and LMS, respectively. The LFP had an orthorhombic structure with *Pmna* space group and also showed impurity phases of FeP, Fe_2P and Li_3PO_4. Similarly, the LMS also had an orthorhombic structure with P*mn2*$_1$ space group and a few impurities of Li_2SiO_3 and MnO which were confirmed using both XRD and FTIR. Furthermore, graphene nanosheets were successfully prepared using the modified Hummer's method. This was evidenced by the fewer number of layers observed in HRSEM and HRTEM images of graphene in comparison to those of graphene oxide. In addition, Raman studies revealed that most oxygen-containing group were removed during the reduction of graphene oxide, therefore successfully forming graphene. Thermal stabilities of these materials were also investigated using thermogravimetric analysis from room temperature to 900 ºC under N_2 atmosphere. It was found that graphene showed higher thermal stabilities attributed to only 38 % weight loss compared to 69 % weight loss for graphene oxide. These precursors were blended together using the two different methods to form LFP-LMS-G and LFP-LMS hybrid cathode materials.

Morphological studies revealed that the LFP-LMS-G had smaller particle sizes compared to LFP-LMS in both preparation methods, which is attributed to the presence of graphene

http://etd.uwc.ac.za

nanosheets during the preparation of these hybrid cathodes. However, LFP-LMS-G prepared via the hand milling approach showed bigger particles (30 ηm) than those prepared using the *in situ* sol-gel approach (23 ηm). This is because the *in situ* sol-gel approach offered better mixing and reaction conditions compared to the hand milling method where the precursors were mixed using a pestle and mortar in an open air environment. Thermogravimetric analysis of the prepared hybrid cathode materials revealed that both hybrid cathodes prepared via the *in situ* sol-gel method were more stable than those prepared using the hand milling method. Again, this further confirms the better mixing offered by this technique.

Electrochemical studies showed successful blending of the pristine cathode materials as evidenced by the presence of iron and manganese redox peaks in the cyclic voltammograms of the hybrid cathode materials. Even though the small contents of graphene were not picked up with XRD, FTIR and Raman spectroscopy the graphenised hybrid cathodes showed better electrochemical properties compared to those without graphene from both approaches. The calculated specific capacities were 4.056, 2.524, 3.408 and 2.804 mA h g^{-1} for LFP-LMS-G SG, LFP-LMS SG, LFP-LMS-G HM and LFP-LMS HM, respectively. These results confirm that the graphenised lithium iron phosphate-lithium manganese silicate hybrid cathode material prepared via *in situ* sol-gel method performed better than that those of the hand milling method. In conclusion, even though these hybrid cathode materials were developed for Li-ion battery applications electrochemical impedance spectroscopy studies revealed that they have a capacitive behaviour. This behaviour is shown by the presence of an inclined line without a semi-circle in the Nyquist plots of these hybrid cathodes.

4.2. Recommendations

This study looked at two different methods that can be used to prepare graphenised lithium iron phosphate-lithium manganese silicate and future works in this research could look at other preparation methods and check the properties and performance of the developed hybrid cathode materials. Furthermore, these studies can also focus on studying the different ratios of the $LiFePO_4$, Li_2MnSiO_4 and graphene that are used to prepare the hybrid cathode materials. Thereafter, the prepared hybrid cathode materials would be used to fabricate coin cells for further electrochemical interrogations.

http://etd.uwc.ac.za